Influence of pin distribution and anodizing on strength of co-bonded joints between additive AlSi10Mg and basalt fibre epoxy composite

Materials & Design 260 (2025) 114967

Contents lists available at ScienceDirect

Materials & Design

journal homepage: www.elsevier.com/locate/matdes

Influence of pin distribution and anodizing on strength of co-bonded joints between additive AlSi10Mg and basalt fibre epoxy composite

Riccardo Miranda [a], Federica Valenza [b,c,d,*], Francesco Di Franco [a], Monica Santamaria [a], Alberta Aversa [b,d], Eleonora Atzeni [c,d], Sara Biamino [b,d], Fabrizio Sarasini [e], Vincenzo Fiore [a]

[a] Department of Engineering, University of Palermo, Viale delle Scienze, 90128 Palermo, Italy
[b] Department of Applied Science and Technology, Politecnico di Torino, Corso Duca degli Abruzzi 24, 10129 Torino, Italy
[c] Department of Management and Production Engineering, Politecnico di Torino, Corso Duca degli Abruzzi 24, 10129 Torino, Italy
[d] Interdepartmental Center of Integrated Additive Manufacturing (IAM@PoliTO), Politecnico di Torino, Corso Castelfidardo 51, 10129 Torino, Italy
[e] Department of Chemical Engineering Materials Environment, Sapienza Università di Roma, Via Eudossiana 18, 00184 Roma, Italy

ARTICLE INFO

Keywords:
Additive manufacturing
Mechanical interlocking structures
Anodizing
AlSi10Mg
Fibre-reinforced composite
Basalt fibres

ABSTRACT

The combination of additively manufactured metallic parts with fibre-reinforced composites offers new opportunities for constructing lightweight, high-performance structures. However, joining dissimilar materials remains challenging due to their differing properties. One promising method is mechanical interlocking, where components are physically interlocked, often via features referred to as pins. This study investigates the effects of macroscopic pin distribution and anodizing treatment on the mechanical strength and corrosion resistance of co-bonded joints. AlSi10Mg substrates, with their surfaces modified to realize pins, were manufactured by powder bed fusion-laser beam process and bonded with basalt fibre-reinforced epoxy composites. Both the influence of four different pin distributions and sulfuric acid anodizing surface treatment were analysed. Results showed that a low pin density (4 × 4 configuration) favoured interlocking, increasing joint resistance and shifting the failure mode from predominantly adhesive to cohesive. Anodizing further enhanced joint resistance, regardless of pin distribution. Polarization curves and electrochemical impedance spectroscopy confirmed that anodizing treatment improves corrosion properties by forming a porous oxide layer, which significantly reduces current density in the passive range. In conclusion, the present paper highlights the combined influence of geometric interlocking and surface treatment in optimizing metal-composite adhesion, providing guidance for advanced structural applications in the aerospace, automotive, and marine industries.

1. Introduction

Polymer Matrix Composites (PMCs) are widely used in many industrial fields due to their ability to provide good mechanical properties while maintaining a low weight. In industrial applications, PMCs are often integrated with metallic parts to obtain higher-performance assemblies that can achieve a wide range of structural and functional properties. Joining these dissimilar materials poses many challenges due to their different mechanical and physical properties. Nowadays, the most common joining technologies are mechanical fastening methods, such as riveting, bolting, and clinching, and adhesive bonding processes, typically involving epoxy-based adhesive [1]. Although widely employed, these approaches present inherent limitations. For instance, mechanical fastening methods, such as riveting, require the creation of holes, which can lead to stress concentration and potentially weaken the material [2]. Adhesive bonding, on the other hand, often involves long curing times and is susceptible to degradation over time or under adverse environmental conditions [2,3]. Consequently, novel joining

Abbreviations: PMC, polymer matrix composite; AM, additive manufacturing; PBF-EB, powder bed fusion-electron beam; CFRP, carbon fibre-reinforced polymer; PBF-LB, powder bed fusion-laser beam; wire-EDM, wire-electrical discharge machining; AB, as-built; SAA, sulfuric acid anodizing; AN, anodized; SEM, scanning electron microscope; EIS, electrochemical impedance spectroscopy; OCP, open circuit potential; EDX, energy dispersive X-ray spectroscopy; EEC, electrical equivalent circuit.

* Corresponding author at: Department of Applied Science and Technology, Politecnico di Torino, Corso Duca degli Abruzzi 24, 10129 Torino, Italy.
E-mail address: federica.valenza@polito.it (F. Valenza).

https://doi.org/10.1016/j.matdes.2025.114967
Received 18 July 2025; Received in revised form 6 October 2025; Accepted 16 October 2025
Available online 19 October 2025

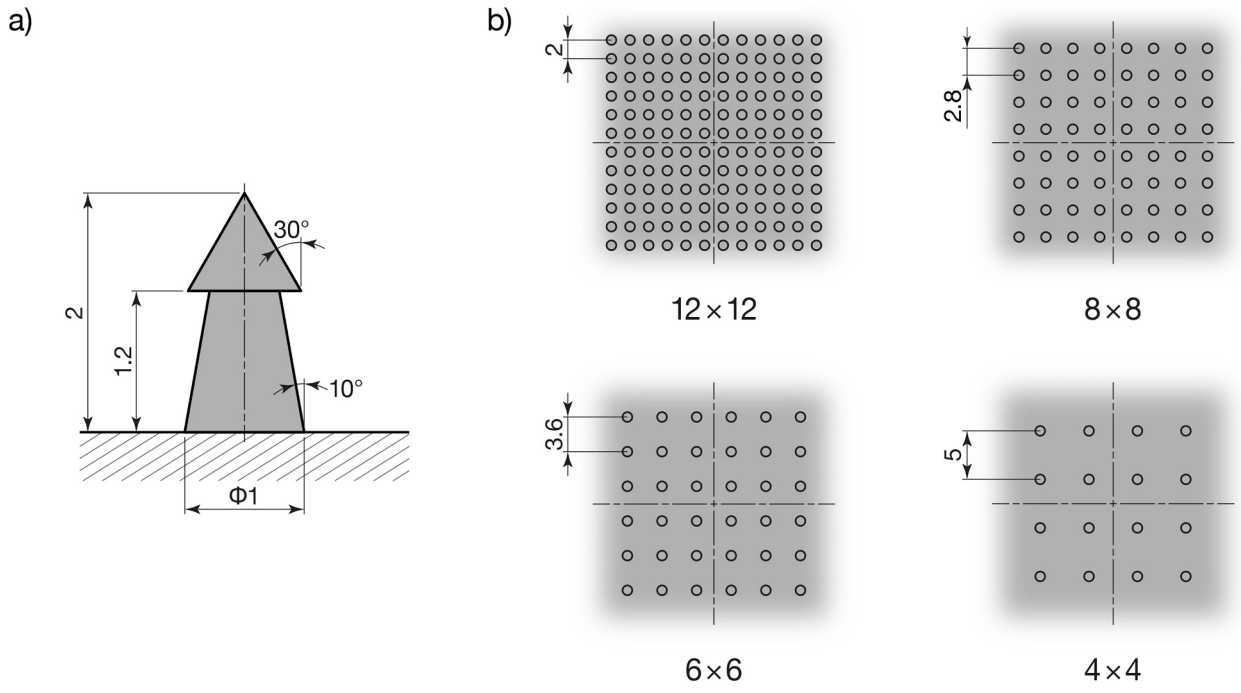

Fig. 1. (a) Pin geometry and (b) spatial configurations. All dimensions are given in millimetres (mm).

technologies are currently under investigation. Among these emerging joining methods, mechanical interlocking is gaining a large interest from many industrial fields thanks to its huge potential. Mechanical interlocking is defined as the joining of parts through a geometrical interlock between components, often involving features such as grooves or protrusions – hereafter referred to as pins. Compared with traditional processes, this method offers high strength and toughness, achieved without the need for additional locking elements or holes, thereby reducing the risk of catastrophic failure [4,5]. Nevertheless, the performance of such joints is still highly dependent on the quality of metal-PMC interface. For this reason, interfacial modification techniques can effectively contribute to enhancing adhesion and promoting more reliable bonding.

The interlocking features can be produced through various conventional processes, such as machining, or by employing Additive Manufacturing (AM) techniques. In particular, AM enables the creation of complex and unique interlocking features that could strongly enhance the joining performance [6]. Furthermore, this would allow joining a PMC substrate together with a metallic component characterised by a topologically optimized design, resulting in a structure that is both high-performing and lightweight.

Consequently, the combination of mechanical interlocking with AM could represent a promising approach for the development of innovative joining solutions [7–10]. As a result, in recent years, many studies have focused on optimizing interlocking features built via AM to achieve the most suitable joining performances. Within this framework, pin geometry, spacing, and surface quality are identified as the primary parameters governing joint performance [11–15].

Sarantinos et al. [15], for example, studied the joining performances of titanium substrates produced via Powder Bed Fusion Electron-Beam (PBF-EB) and Carbon Fibre-Reinforced Polymer (CFRP). The study considered three different pin geometries and demonstrated that the pin shape significantly influences the joint load-bearing behaviour and failure mechanisms. Notably, the introduction of undercut features resulted in the maximum pull-out force and energy absorption. Similar results were obtained by Parkes et al. [16] on Ti6Al4V components fabricated by Powder Bed Fusion Laser-Beam (PBF-LB) and CFRP joints. The authors confirmed that the conical head of the arrow-shaped pin enables effective embedding and anchoring of the fibres, providing an enhanced mechanical interlock. Graham et al. [17] worked on the joining performance of AISI 316 with glass fibre-reinforced polymer, demonstrating that an optimized pin distribution can reduce stress concentration and minimize the disruption of the fibre architecture. Furthermore, an effective pin distribution can shift the failure regime, promoting a more ductile failure mode, while increasing energy absorption and improving the overall joint performance. These findings align with those of Woitun et al. [11], who highlighted that achieving uniform stress distribution, through evenly distributed surface features, is a key factor for enhancing bond strength.

Ultimately, when coupling dissimilar materials, surface properties – particularly surface roughness – also play a crucial role. This occurs because surface roughness enhances the effective contact area between the materials, enabling one material to mechanically interlock with the surface asperities of the other, thereby improving adhesion [18]. Therefore, several studies have focused on tailoring surface roughness through the modification of AM process parameters or through post-processing treatments to promote the activation of the micro-interlocking mechanism, which depends on the presence of micrometric surface features. In this regard, some authors found that an anodizing treatment could strongly improve joining performances due to the formation of a nanoporous oxide structure, which enables effective infiltration between dissimilar materials [12]. For example, Zhao et al. [19] studied the bonding strength of polyphenylene sulphide to aluminium alloy using constant current anodizing in tartaric acid. The optimal bonding strength (25 MPa) was achieved with 120 A/m^2 current density, 30 min anodizing, and 45 min etching, resulting in anodic aluminium oxide films with balanced roughness and porosity. Similarly, Tseng et al. [2] investigated anodized AA5052 surfaces patterned with biomimetic microstructures and bonded with CFRP. In their work, anodization was carried out in 10 % sulfuric acid solution at 12 V for 30 min, producing a porous oxide layer that enhanced adhesion and provided a more stable interface.

It is well known that the anodizing process also leads to an increase in the corrosion resistance [13]. Accordingly, the anodizing process of the metallic component prior to interlocking can lead to improvements in joint quality and corrosion resistance, which is particularly relevant given that galvanic corrosion has been reported between certain PMCs

and metallic substrates [14]. This is a relevant issue for the aerospace, automotive and marine industries, in which the joint components are often exposed to corrosive environments [20]. However, nowadays, anodizing materials processed via AM presents a significant challenge due to their unique microstructure. For example, Revilla et al. [21,22] investigated the anodizing behaviour of Al-Si alloy samples produced via the PBF-LB method. They discovered that the silicon particles, being significantly smaller than those of the same alloy in the as-cast condition, underwent complete oxidation. As a result, a substantial amount of the anodic charge was consumed during the process, leading to a much slower growth rate of the anodic layer in the PBF-LB samples compared to the cast alloy.

The present work aims to characterize interlocking joints between epoxy-based composites reinforced with basalt fabrics and AlSi10Mg substrates built via AM. Basalt fibres were chosen to reinforce the composite substrates due to their natural origin, less energy-intensive production, and superior environmental profile compared to glass and carbon fibres [23]. Additionally, their high mechanical properties, good temperature resistance, chemical stability, and excellent thermal and acoustic insulation make them a highly desirable reinforcement material [24,25]. AlSi10Mg was chosen due to its excellent strength-to-weight ratio, making it well-suited for lightweight applications [26]. The novelty of this study relies on the combination of these materials with a systematic investigation of two key factors to optimize joint performance: (1) the effect of macroscopic pins and their distribution on fibre interlocking and bond strength, and (2) the impact of electrochemical surface treatment on adhesion and corrosion resistance. Conceived as a feasibility study, it is intended as an important first step towards future optimization of metal-composite joining process, with relevance for lightweight and environmentally conscious structural applications.

2. Materials and methods

2.1. Design and distribution of the mechanical interlocking structures

In the present study, a refinement of the arrow-shaped pin design reported in the literature [15,16] was proposed (Fig. 1a). The defined geometry, consisting of a conical tip and a truncated-cone body, was designed on the basis of demonstrated advantages [15,16,27]. First, the conical tip has been proven to facilitate embedding into composite materials without damaging the fibres, an issue commonly encountered with traditional bolted joints [15]. Additionally, the undercut geometries created by the truncated-cone body are expected to enhance fibre interlocking, resulting in superior ultimate load capacity compared to simple cylindrical pins [15]. The pin dimensions were defined in the millimetric range to optimize production efficiency while ensuring robust interlocking performance.

To examine the effect of pin distribution within the overlap region between the PMC and the metal substrate, four different configurations were investigated. In detail, pins were arranged in a square matrix within a 25 × 25 mm^2 overlap region, distributed across the following configurations: 12 × 12, 8 × 8, 6 × 6, and 4 × 4 arrays (Fig. 1b). The inter-pin spacing, measured as the distance between the symmetry axes of two adjacent pins, systematically varied from 2 mm in the most densely packed configuration to 5 mm in the least dense arrangement. Increased inter-pin spacing resulted in a corresponding decrease in the total number of pins, yielding evenly distributed arrays.

2.2. Materials and production

The metal substrates were manufactured using the EOS M270 Dual Mode PBF-LB machine with AlSi10Mg spherical powder, comprising particle sizes ranging from 25 μm to 80 μm. Both the machine and the powder were supplied by EOS GmbH (Krailing, Germany). The process was conducted under a continuous argon flow, with the oxygen level in the building chamber maintained below 0.1 %. The platform temperature was kept at 100 °C. The scanning strategy involved the use of stripes with a width of 5 mm and a rotation of the scanning vector by an angle of 67° between consecutive layers. The process parameters are illustrated in Table 1. After the production, the samples were subjected to a stress-relieving heat treatment at 290 °C for 1 h. Subsequently, the samples were separated from the building platform using the Wire-Electrical Discharge Machining (wire-EDM) e-cut system by Suzhou Baoma (Suzhou, China).

Table 1
Process parameters employed for AlSi10Mg with the EOS M270 Dual Mode system.

Parameters	Value
Laser power	195 W
Laser spot size	100 μm
Layer thickness	30 μm
Hatching distance	0.17 mm
Scanning speed	800 mm/s

The metal components realized for this study measured 80 × 25 × 2 mm^3 (Fig. 2). This design was developed in accordance with the ASTM D1002 standard for single lap shear test of adhesively bonded specimens. However, since the present work focuses on mechanical interlocking rather than adhesive bonding, and considering the dimensional requirements of the AM process, the standard geometry was adapted accordingly, reducing its dimensions while preserving the overall shape.

As described in the previous section, each specimen exhibited a 25 × 25 mm^2 side area where pins were arranged in four distinct configurations. To ensure statistical reliability in the experimental analysis, 8 replicas for each configuration were produced, for a total of 32 samples.

The PMC substrate was fabricated using a 13-layer lay-up of bi-directional woven plain basalt fabric with an areal weight of 220 g/m^2, supplied by Basaltex NV. Specifically, the cross-ply [0°/90°] stacking sequence has been chosen. This fabric was previously silane-treated with (3-Aminopropyl)trimethoxysilane and combined with an epoxy matrix obtained by mixing (weight ratio 100:22) a bio-epoxy monomer (Polar Bear) with an amine-based hardener (Recyclamine™ R*101), both supplied by R*Concept.

The fibre volume fraction of the manufactured composite was equal to 37 %. This value was calculated through equation (Eq. (1)):

$$v_f = 100 \times \left(\frac{n \times m}{\varrho_f \times t}\right) \quad (1)$$

where n is the number of fabric layers, m is the fabric nominal areal weight, ρ_f is the density of basalt fibres (i.e., 2.67 g/cm^3), and t is the composite thickness.

Classified as bio-based, this epoxy matrix exhibits a bio-carbon weight content exceeding 28 % and is recyclable. The chemical recyclability of the thermoset matrix stems from the nature of the hardener, which is a “cleavable” amine capable of opening the cross-links when the composite is soaked in a mild acid solution under specific conditions [28–30] (e.g., temperature, solution concentration, and immersion time). By following this procedure, a complete recovery of the reinforcement is achievable, as the epoxy matrix transforms into a thermoplastic material and precipitates out of the solution.

2.3. Aluminium alloy surface treatments

In this study, the anodizing electrochemical technique was utilized to bolster the interlocking mechanism between the aluminium alloy surface and the polymeric composite and to enhance the corrosion resistance. The samples, with the as-built (AB) surface roughness resulting from the AM process, were ultrasonically degreased in acetone for 5 min. The process involved immersing the sample in a stirred aqueous solution containing 3 M sulfuric acid (H_2SO_4) within a cell setup consisting of a galvanostat and an aluminium counter electrode, following the general

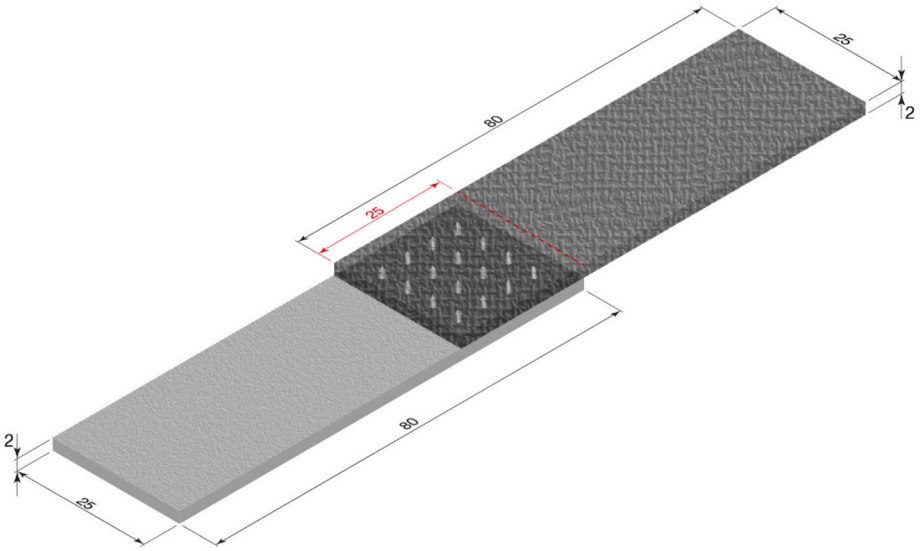

Fig. 2. Geometry of the single lap shear specimens, with the composite in transparency to evidence mechanical interlocking structures and the overlap zone highlighted in red.

Table 2
Denomination of the tested samples.

	12 × 12	8 × 8	6 × 6	4 × 4
As-Built	12-AB	8-AB	6-AB	4-AB
Anodized	12-AN	8-AN	6-AN	4-AN

anodizing scheme reported in [2]. A constant current density of 10 mA/cm^2 was applied for a duration of 20 min, rendering the process galvanostatic. Hereafter, the Sulfuric Acid Anodizing surface treatment is referred to as SAA.

Four specimens out of the eight replicas per each pin configuration were anodized in sulphuric acid (AN). The denomination assigned to the specimens, reflecting the different spatial configurations and surface conditions investigated, is reported in Table 2.

2.4. Surface morphology analysis and corrosion resistance measurements

The porous layer structure formed during the anodizing process underwent examination using a FEI Quanta 200 FEG scanning electron microscope (SEM). By comparing the morphologies of all samples before and after the electrochemical process, microstructural differences were examined.

To evaluate the corrosion resistance, Electrochemical Impedance Spectroscopy (EIS) was employed. The samples were submerged in a 3.5 % NaCl solution and linked to a Parstat 2273 potentiostat, configured in a three-electrode setup comprising the sample, a platinum counter, and an Ag/AgCl reference electrode. Initially, the open circuit potential (OCP) was monitored within the cell for 60 min. Subsequently, EIS measurements were conducted by applying a sinusoidal potential with a ±10 mV amplitude relative to the OCP value, while varying the frequency from 100 kHz to 100 mHz.

Finally, a polarisation curve was recorded, again in the same solution, from −200 mV relative to the OCP value until 1 V to assess the effect of the various electrochemical treatments on potential, corrosion current, and passivity current.

2.5. Fabrication of the joint

Single lap co-bonded joints were manufactured via vacuum infusion, allowing the composite to be produced and joined to the metallic substrate in a single step [31]. Four metallic substrates, in AB or AN condition, were positioned in a plain mould, dry basalt fabrics were arranged over them within the pinned area, and the assembly was placed in a vacuum bag. Subsequently, the epoxy matrix was infused into the setup, driven by the pressure differential between the vacuum bag and the surroundings. The curing phase lasted for 24 h at room temperature under vacuum conditions, ensuring simultaneous curing of the resin and bonding to the metallic surfaces. Samples were then post-cured in an oven at 100 °C for 3 h. No additional complexities were introduced into the manufacturing process to maintain conditions as close as possible to conventional co-bonded joint fabrication.

Finally, the single lap specimens were cut using a Bosch GCM 800 SJ rotary blade to remove the excess material. The ultimate geometry of the samples is illustrated in Fig. 2.

2.6. Single lap shear test

All the specimens were subjected to single lap shear tests, utilizing the geometry depicted in Fig. 2. A universal testing machine, Wance model ETM-C, equipped with a 50 kN load cell, was utilized for this purpose. A crosshead speed of 1.27 mm/min was employed. Comparison of maximum load resistance (kN) was conducted across specimens, as lap-shear stress (MPa) could not be evaluated owing to the three-dimensional geometry of the joint surface. Moreover, using nominal stress would not provide further insight, since the actual contact area is modified by pins and anodizing and the load is not uniformly distributed across the overlap, potentially introducing uncertainties.

Additionally, visual inspections were conducted post-testing to assess any observable differences in the failure modes between the specimens. Fracture surfaces were imaged using a Leica S9i stereomicroscope (Leica Microsystems, Wetzlar, Germany) equipped with a digital camera, at a ×10 magnification under reflected light. The acquired micrographs were subsequently processed through digital image analysis in ImageJ (v1.54 g, National Institutes of Health, Bethesda, MD, USA). Threshold-based segmentation was applied to distinguish the different fracture modes, and the corresponding area fractions were quantified relative to the total overlap area.

3. Results and discussions

3.1. Morphology of the AM surfaces and the effects of anodizing

SEM micrographs were useful to evaluate the morphology of the AM

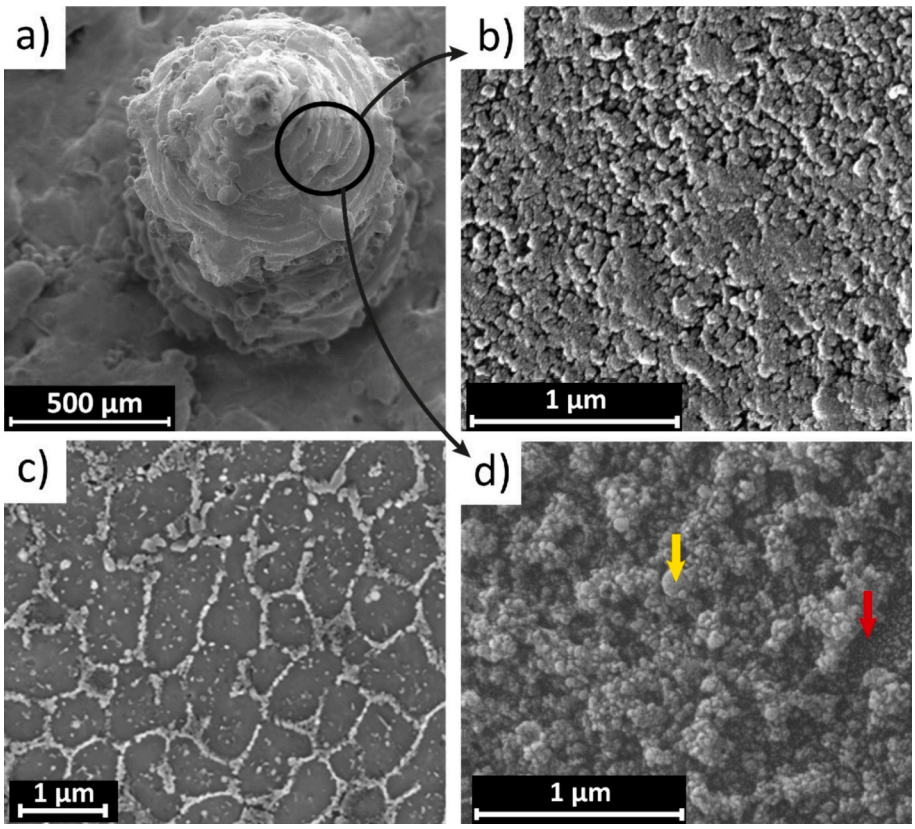

Fig. 3. SEM micrographs of a) the single AB pin; b) surface morphology of the AB pin edge at 100 kX magnification; c) microstructure of the XZ cross section of an AB sample; d) surface morphology of the AN pin edge at 100 kX magnification.

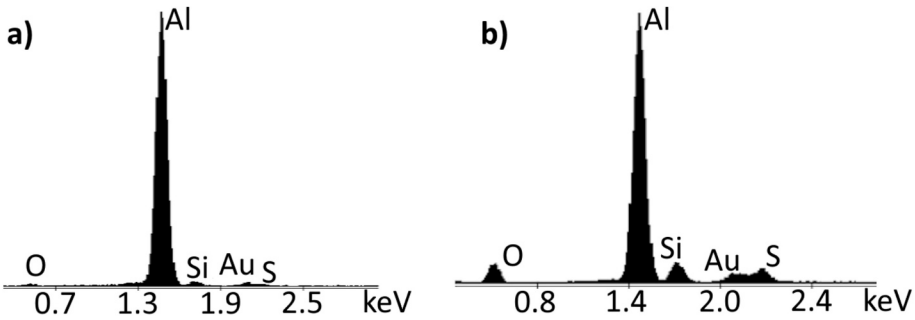

Fig. 4. EDX results on the pin edge: a) AB; b) AN.

surface with the pins and how the anodizing process changed it. In Fig. 3a, the macroscopic morphology of the samples is very discontinuous and rough, especially the surface of the individual pin, highlighting the limits of the AM system in producing such detailed small-scale features. These observations are in line with a previous study [32] based on computed tomography analysis, which revealed small deviations between the nominal and actual geometry, mainly due to shrinkage and balling phenomena, and particularly affecting fine details such as the arrow tip. Moving to high magnification, in Fig. 3b, it can be noted that the AB pin surface appears homogeneous. Regarding the chemical composition, a non-complete uniformity with very fine silicon rich regions distributed on the surface is observed looking at the microstructure of the AlSi10Mg samples which is made of α-Al cells surrounded by a fine Si eutectic network (Fig. 3c). The surface morphology changes because of the anodizing (Fig. 3d) and two different structures can be distinguished. The brighter part (highlighted by the yellow arrow) is the silicon that undergoes an oxidation process during anodizing, while the darker part (highlighted by the red arrow) is the porous alumina layer that develops during anodizing. The PBF-LB samples do not generate an oxide layer easily distinguishable as it happens in the cast aluminium alloy. In addition, the presence of silicon influences the anodizing process, because part of the anodizing current provided is used to oxidise the silicon itself, instead of growing the desired porous alumina layer [21].

All the chemical species are evidenced in the Energy Dispersive X-ray Spectroscopy (EDX) results, visible in Fig. 4. The region of interest for the EDX spectrum, indicated by the black circle in Fig. 3a, is the same for AB and AN samples. In the AN samples (Fig. 4b), there was the presence of sulphur, due to the anodizing bath and oxygen for the formation of aluminium and silicon oxides. The content of these two elements was almost negligible in AB samples.

Overall, the morphology and EDX results indicated that the anodizing process impacts the samples. To further demonstrate the effectiveness of anodizing, corrosion and mechanical tests were carried out.

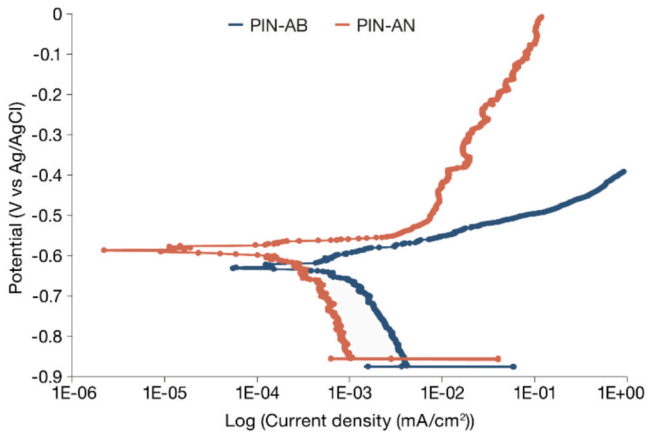

Fig. 5. Polarization curves of PIN-AB and PIN-AN samples.

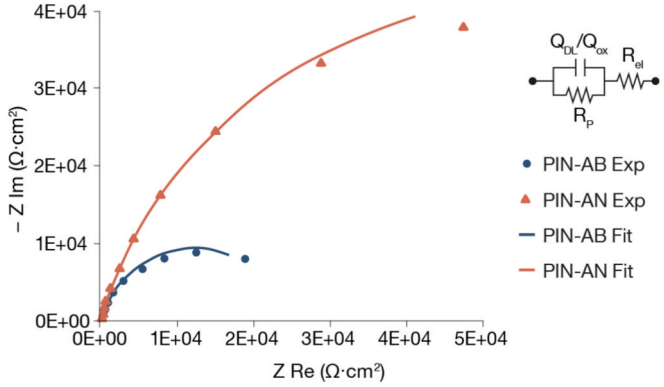

Fig. 6. EIS spectra in Nyquist representation of PIN-AB and PIN-AN.

3.2. Corrosion resistance

To assess the corrosion resistance of the examined metallic substrates and their correlation with the resulting oxide morphology, polarization curves and EIS spectra were obtained in a 3.5 wt% NaCl aqueous solution, simulating seawater, an extremely aggressive environment for aluminium alloys. As the corrosion measurements were normalized for the actual immersed area and the distribution of pins did not affect the tests, only 12 × 12 samples were used in Fig. 5 to compare the corrosion results before and after the anodizing process. For simplicity, the names PIN-AB and PIN-AN, corresponding to 12-AB and 12-AN, respectively, were used to generalize the sample types.

The potentiodynamic polarization curves for PIN-AB and PIN-AN samples are presented in Fig. 5.

The anodizing process significantly influences the current density in both the anodic and cathodic branches. As depicted in Fig. 5, it is worth noting that the anodizing (PIN-AN) shifts the corrosion potential to more positive values and reduces the current density in the passivity region by two orders of magnitude. These results demonstrate an improvement in the corrosion resistance of the PIN-AN samples compared to the PIN-AB and are also supported by EIS results.

Nyquist plots, resulting from EIS measurements at OCP, are shown in Fig. 6.

The spectra exhibit depressed semicircles, with their diameter depending on the surface treatment. Specifically, these spectra were modelled using the Electrical Equivalent Circuit (EEC) shown in the insert of Fig. 6, which consists of the electrolyte resistance (R_{el}) in series with a parallel RQ circuit, where Q represents a constant phase element used to account for the non-ideal capacitive behaviour of the interface. In PIN-AB, this element corresponds to the double-layer capacitance (Q_{DL}), whereas in PIN-AN, it represents the charge stored in the barrier alumina layer (Q_{OX}). This difference was required because the PIN-AB had no protective oxide layer other than the naturally formed one, whose thickness is negligible. In both cases, the constant phase element is placed in parallel with the polarization resistance (R_p). The EIS spectra fitting parameters for PIN-AB and PIN-AN samples are summarized in Table 3.

Table 3
Fitting parameters derived from EIS results.

	R_{el} (Ω cm^2)	R_p (Ω cm^2)	Q_{DL}, Q_{OX} (S s^n cm^{-2})	n	d_{ox} (nm)
PIN-AB	25.6	2.4×10^4	3.6×10^{-5}	0.83	–
PIN-AN	32.2	1.1×10^5	1.8×10^{-5}	0.81	2.46

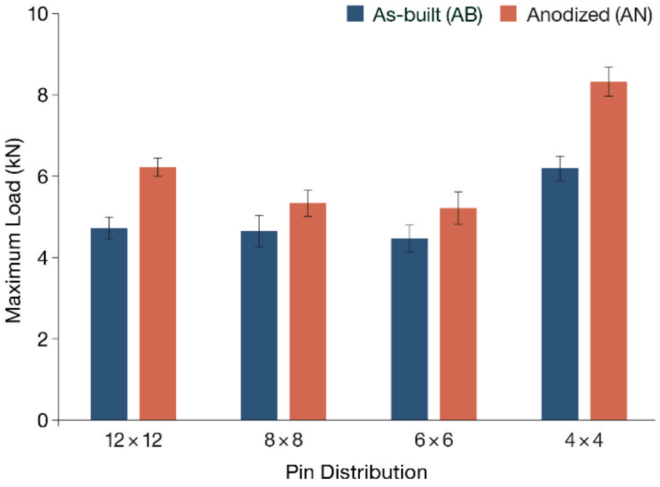

Fig. 7. Maximum load exhibited during single lap shear test at varying pin distribution and surface treatment. Values represent the average maximum load of the four specimens per configuration; error bars indicate the standard deviation.

Experimental results evidenced that the polarization resistance of PIN-AN is higher than that of PIN-AB samples, confirming the higher corrosion resistance already evidenced by polarization curves (Fig. 5).

Valuable insights can also be gained from the modulus of the constant phase element and its exponent n. The Q_{ox} values obtained from the fitting parameters allow for the estimation of the barrier layer capacitance, C_{ox}, using the Brug formula (Eq. (2)), as detailed by Hirschorn et al. [33]. The barrier layer thickness, d_{ox}, can be calculated starting from C_{ox}, and aluminium oxide dielectric constant, $\varepsilon = 9$, as follows (Eq. (3)) [34]:

$$C_{ox} = \frac{(R_{el}Q_{ox})^{\frac{1}{n}}}{R_{el}} \tag{2}$$

$$d_{ox} = \frac{\varepsilon_0 \varepsilon}{C_{ox}} \tag{3}$$

where ε_0 is the vacuum permittivity.

The results reported in Table 3 evidenced that the anodizing treatment on this particular form of aluminium alloy surface generated an oxide layer a few nanometres thick, which protects the metal substrate from the aggressive environment. In contrast, the untreated aluminium alloy remains more susceptible to corrosion. Overall, this paper showed that anodizing can create a porous layer even in additively manufactured specimens with complex three-dimensional shapes, protecting them from corrosion and enhancing mechanical performance, as highlighted in the following paragraphs.

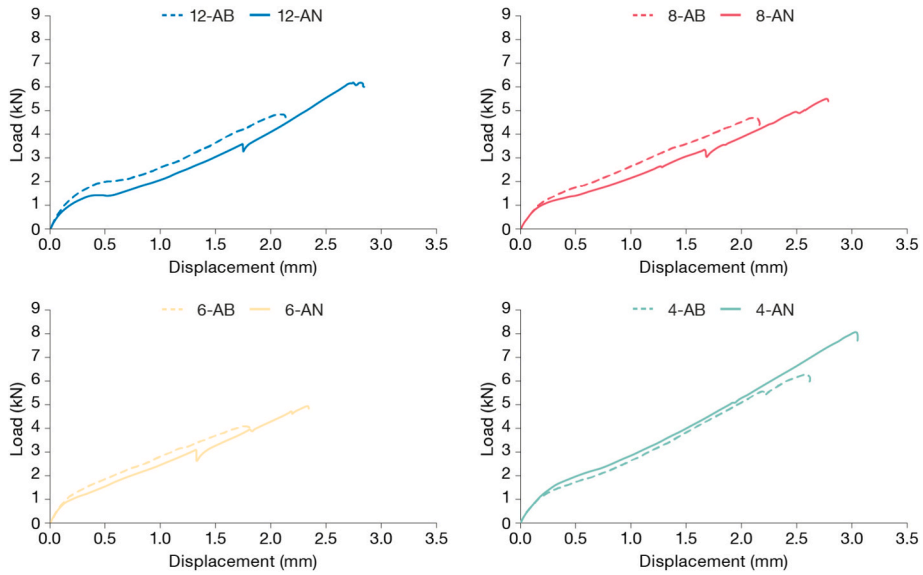

Fig. 8. Load–Displacement curves of AB and AN samples for each pin distribution.

3.3. Single lap shear tests

The results of single lap shear tests performed on specimens varying the distribution of pins with and without anodizing are shown in Fig. 7.

The first noteworthy result is that surface modification via the anodizing process led to an increase in resistance, regardless of the pin distribution. Considering the maximum load, calculated as the average of the four specimens tested for each configuration (Fig. 7), 12-AN reached 6.2 ± 0.2 kN, corresponding to a 31 % improvement over 12-AB (4.7 ± 0.3 kN). Likewise, 8-AN and 6-AN yielded 5.3 ± 0.3 kN and 5.2 ± 0.4 kN, with increases of 15 % and 18 % over their AB counterparts (4.6 ± 0.4 kN and 4.4 ± 0.3 kN, respectively). Finally, the samples that exhibited the highest increase were 4-AN, which achieved 8.3 ± 0.3 kN, representing a 34 % increase compared to 4-AB (6.2 ± 0.3 kN).

A further finding indicates that high pin distribution correlates with reduced resistance. In fact, 12-, 8-, and 6-AB (as well as 12-, 8-, and 6-AN) samples reported similar values of maximum load. However, decreasing the distribution from 12 × 12 to 4 × 4 led to approximately 31 % and 34 % increase in maximum load for AB and AN samples, respectively. Even among the differences between AB and AN, the 4 × 4 configuration yielded the best results. While the overall trend confirms the beneficial effects of reduced pin density and anodizing treatment on joint strength, minor deviations from the expected positive progression were observed. Specifically, the 12-AN configuration displayed a maximum strength exceeding that of intermediate pin densities (8-AN and 6-AN). This anomaly may be attributed to possible non-systematic local variations occurring during the joint manufacturing process. Moreover, this behaviour may also be related to the compensating effect of a greater number of anchoring points, which could contribute to the load-bearing capacity in configurations where the effect of mechanical interlocking is limited.

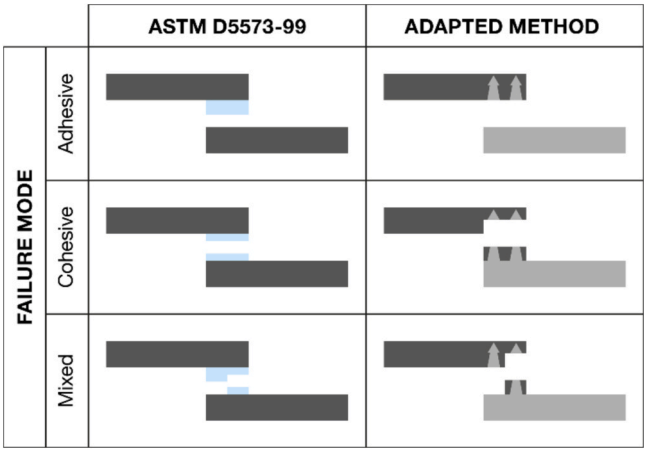

Fig. 9. Failure mode classification based on ASTM D5573-99 (left column) and the corresponding adaptation developed for the paper case study (right column).

Fig. 8 reports the load–displacement curves for each pin distribution, directly comparing AB and AN cases. Shear strength is expressed as load (kN) rather than the nominal shear stress (MPa), since all configurations share the same overlap area and a normalization would not change the trends. By contrast, the effective contact area, affected by pin density and anodizing, cannot be determined with sufficient accuracy. Moreover, as reported in literature [17], load transfer is non-uniform across the overlap. The curves shown are the most representative of each configuration; in all cases, the four replicates exhibited nearly overlapping responses.

Analysing the graphs, it can be observed that across all configurations, the initial slope is comparable, indicating similar joint stiffness; in line with literature [35], pins do not significantly affect the initial stiffness. Anodizing, however, shifts the curves to higher peak loads and larger displacements at failure. In the 12-AN configuration, the average displacement at maximum load reached 2.6 ± 0.1 mm compared to 2.2 ± 0.3 mm in 12-AB, corresponding to an increase of 18 %. Similar improvements were observed in 8-AN and 6-AN, which reached 2.7 ± 0.4 mm and 2.4 ± 0.3 mm compared to 2.2 ± 0.2 mm and 2.0 ± 0.4 mm, with increases of about 23 % and 20 %, respectively. Finally, 4-AN achieved 2.9 ± 0.3 against 2.6 ± 0.2 mm in 4-AB, with a 12 % increase. In addition, AN curves display a more progressive failure, while AB responses tend to drop more abruptly. This further confirms the beneficial effect of anodizing: such behaviour is consistent with enhanced interfacial adhesion, that allows crack-bridging at the interface, delays debonding, and increases energy absorption [35].

The influence of pin distribution remains evident also in these load–displacement profiles: the lowest areal density attains the largest peak load and the widest stable extension before rupture, while denser patterns provide smaller gains. Reducing the distribution from 12- to 4-, in both AB and AN cases, led to an increase in maximum displacement of respectively 18 % and 12 %. The improvements in displacement in the

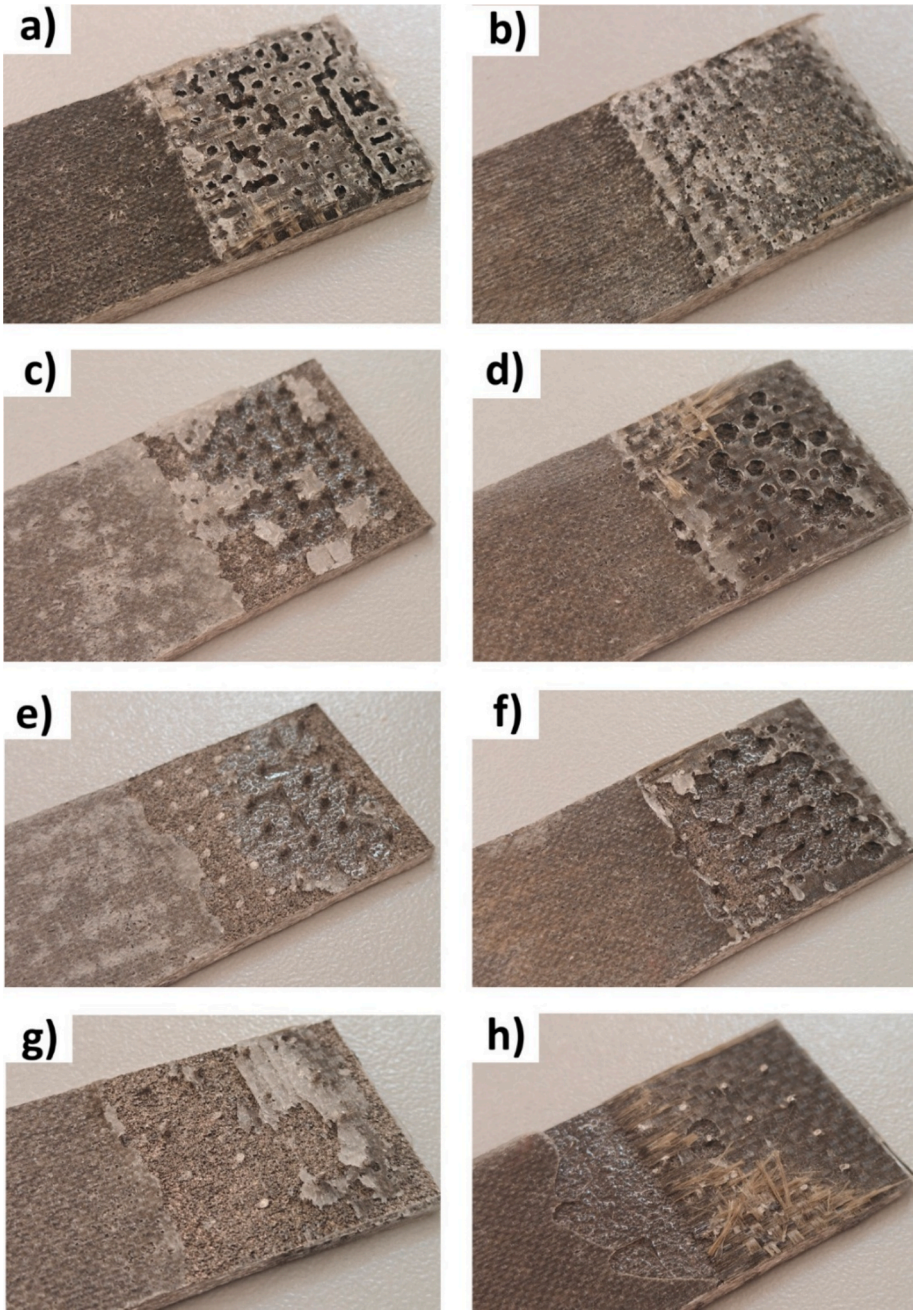

Fig. 10. Rupture surfaces of samples AB and AN: a) 12-AB; b) 12-AN; c) 8-AB; d) 8-AN; e) 6-AB; f) 6-AN; g) 4-AB; h) 4-AN. Dimensional details are consistent with those provided in Figs. 1–2.

AB series were more pronounced when reducing the pin density; while in the AN series the effect was more evident for the intermediate distributions, as the 4 × 4 configuration already achieved the largest deformation capacity.

In summary, both anodizing and pin distribution significantly affect the mechanical response. In terms of deformation capacity, the effect of anodizing is more evident, enabling maximum increases of about 23 % and promoting a more progressive failure mode. For maximum load, instead, anodizing and pin distribution exert a comparable influence, leading to maximum increases of about 33–34 % when anodizing is coupled with the lowest pin density, suggesting that this pin distribution is the one, among the investigated ones, that better fits with the basalt fabric used in this work.

To understand the mechanisms leading to these different behaviours, the fracture surfaces of the samples were observed. The analysis was conducted following the ASTM D5573-99 (2019) standard, which provides a systematic classification of failure modes based on visual inspection. Although this standard is intended for adhesively bonded fibre-reinforced PMC joints, it was adapted here to evaluate mechanical interlocking joints between AlSi10Mg alloy and basalt-PMC substrate (Fig. 9).

The fracture analysis revealed that all samples exhibited mixed failure modes, comprising both adhesive and cohesive failures (Fig. 10). Adhesive failure refers specifically to the separation occurring at the interface between the adhesive and the adherend, which here corresponds to the interface between the resin matrix and the metal substrate (Fig. 9). Cohesive failure, conversely, refers to a fracture within the adhesive itself; in the present context, this is represented by fractures occurring within the composite structure (Fig. 9).

In the fracture analysis, it is essential to distinguish between the

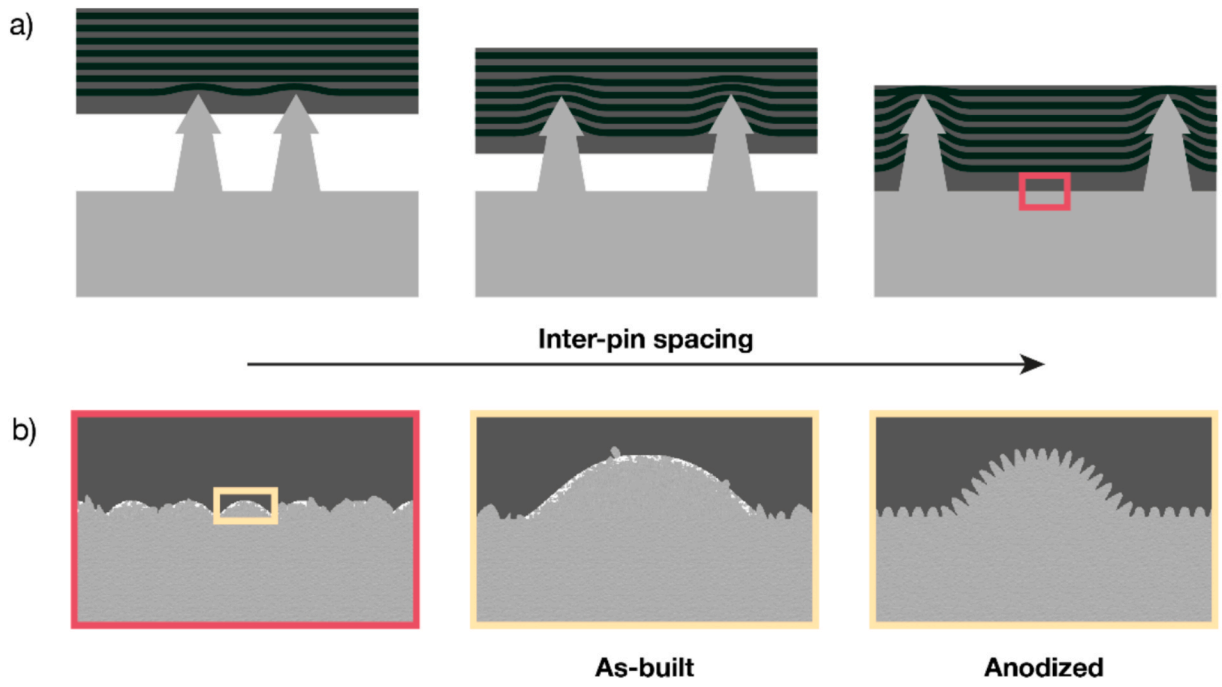

Fig. 11. a) Effect of reduced inter-pin spacing on composite penetration; b) effect of surface treatment on metal-composite adhesion (dimensions are not to scale and are shown for illustrative purposes only).

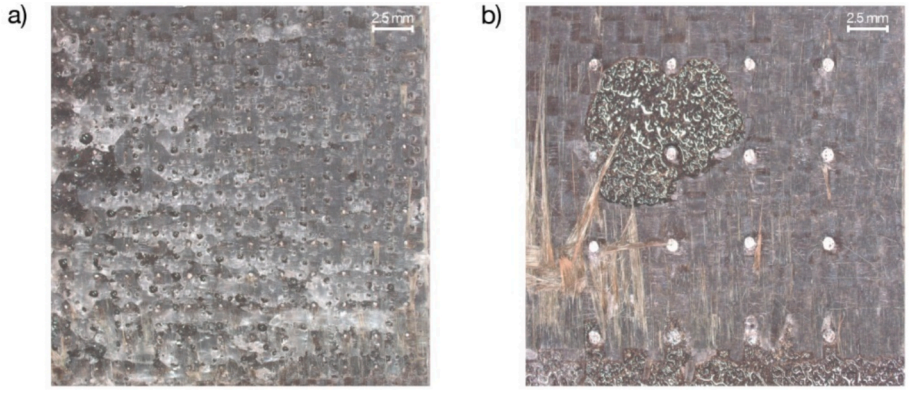

Fig. 12. Comparison between fracture morphologies of two representative configurations: a) 12 × 12 AN, showing a continuous resin layer covering the pins, and b) 4 × 4 AN, showing a mixed fracture with adhesive and cohesive regions, fibre tear, and fractured pins.

effects related to pin distributions and those resulting from the anodizing treatment. The effect of pin distribution was clearly evident from visual inspection. In the high-density configurations – 12 × 12 and 8 × 8 – the reduced inter-pin spacing hindered the effective penetration of the composite into the interlocking structures. This led to a stratified structure: a layer of densely packed pins with poor resin infiltration, followed by a resin-rich layer above the pin tips, and the composite reinforced region (Fig. 11a). Visual inspection of these specimens prior to single lap shear test confirmed this structure, revealing good adhesion at the overlap region edges, but a noticeable swelling in the central area with the pins. During fracture, almost all pins remained intact, and failure mainly occurred within the resin-rich layer above the pin tips (Fig. 10a-d). This correlates with the lower maximum strength values measured for these configurations (Fig. 7). In the 6 × 6 configuration, the reduced pin density allowed slightly improved composite infiltration (Fig. 11a), although the central part of the overlap region still appeared insufficiently wetted by the resin. In this case, a mixed failure was observed, predominantly adhesive (Fig. 10e-f). Finally, in the configuration with the lowest pin density (4 × 4), a complete composite infiltration was achieved (Fig. 11a), resulting in full engagement of the pins during loading and subsequent fracture (Fig. 10g-h). This thorough integration contributed directly to an observable increase in maximum strength, underscoring the essential role of pins and their distribution in promoting mechanical interlocking and effective stress transfer.

These qualitative observations were complemented by post-testing digital image analysis, which enabled quantification of the area fractions associated with cohesive and adhesive failures. For the 12 × 12 and 8 × 8 configurations, stereomicroscope inspection confirmed the inadequate composite penetration, with a resin layer visible above the intact pin tips (Fig. 12a). Since the failure mechanisms in these cases were dominated by the resin-rich layer rather than by effective adhesive or cohesive modes, they were excluded from quantitative image analysis.

For the 6 × 6 and 4 × 4 configurations, instead, it was possible to measure the relative fractions of failures (Fig. 12b). The 6 × 6 specimens exhibited mixed failure, with cohesive fracture areas of 14.6 ± 5.6 % (AB) and 42.6 ± 13.5 % (AN) (Fig. 13). This outcome reflects partial resin penetration, with some pins engaged during loading, but not enough to significantly change the overall load-bearing mechanism,

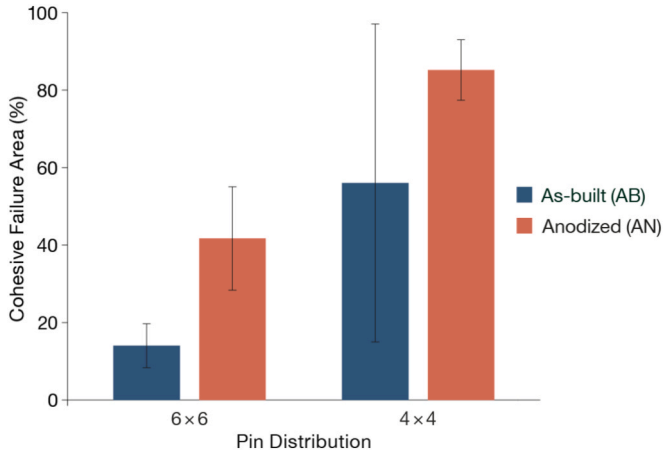

Fig. 13. Cohesive fracture area (%) over the overlap for 6 × 6 and 4 × 4 configurations. Values correspond to the mean fraction of the four replicates for each configuration, with error bars as standard deviation. Only the cohesive fraction is reported, as the adhesive contribution is its complementary.

which remained largely sustained by the resin matrix. Accordingly, the maximum strength values were similar to those of the denser configuration (Fig. 7). By contrast, the 4 × 4 configuration showed a much higher degree of interlocking efficiency, with cohesive fracture areas of 57.4 ± 41.6 % (AB) and 86.6 ± 7.9 % (AN) (Fig. 13). In both AB and AN specimens, fibre tear was also detected, amounting to about 15.0 % of the cohesive area, which is indicative of a stronger and more robust joint. Nevertheless, a high standard deviation was observed for the 4-AB specimens, suggesting variability likely related to manufacturing process conditions. Although similar sources of non-repeatability may occur in all configurations, their influence appeared to be amplified in the 4-AB case, where the lower pin density leaves a larger fraction of the interface unsupported by mechanical interlocking, making failure modes more sensitive to local process-related defects.

Evaluating the influence of anodizing treatment, a clear enhancement of composite-metal adhesion was observed, affecting both substrates and pin surfaces (Fig. 11b). Consequently, AN specimens consistently showed a higher proportion of cohesive failure across all pin distributions compared to their AB counterparts, indicating improved bonding (Fig. 10f-h and Fig. 13). This is particularly evident in the 4 × 4 configuration (Fig. 10h), where the 4-AN specimens yielded the highest maximum strength and the largest cohesive fracture area among all tested combinations (as shown in Fig. 7, Fig. 8, and Fig. 13). Moreover, anodizing reduced the standard deviation of the measured cohesive fracture area (Fig. 13), indicating a more reproducible behaviour. This may be attributed to the more controlled surface condition provided by the porous anodized oxide layer, which increased the effective surface area and facilitated resin infiltration and fibre interlocking during processing, thereby reducing process-dependent variability.

These findings clearly indicate that the combined effect of optimized pin distribution and anodizing treatment promotes effective mechanical interlocking and enhanced interfacial adhesion, thereby increasing the actual contact surface area and resulting in superior mechanical performance, a more progressive fracture, and a higher percentage of cohesive failure.

Finally, focusing specifically on interlocking features performance, it was observed that pin rows adjacent to internal overlap edges broke in all configurations, aligning with literature identifying this zone as prone to stress concentration [17,36]. As previously discussed, this is also justified by the fact that high pin density impeded effective resin penetration, leading to central swelling and stronger lateral adhesion at specimen edges. Furthermore, with a reduction in pin density, nearly all pins participated actively in the failure process, fracturing approximately at their mid-section, just beneath the tip, in both AN and AB configurations (Fig. 14a-c). In this case, the pin heads remain embedded in the composite substrate after rupture, as exemplified by the 4 × 4 configuration in Fig. 14b, confirming the effectiveness of the interlocking mechanisms. Nevertheless, this fracture location underscores that although undercut geometry effectively anchors composite fibres, it simultaneously creates a region susceptible to fracture due to abrupt geometric transitions. Therefore, refining the arrow-shaped geometry may represent a promising direction for future studies.

In conclusion, when using the vacuum infusion joining technique in combination with a composite reinforced with high areal weight fibre fabrics, reduced pin density facilitates resin infiltration and full engagement of interlocking mechanisms. In this way, decreasing pin density from 12 × 12 to 4 × 4 allowed transitioning the primary resistance mechanisms from resin-dominated, at high densities, to an optimized synergy of resin adhesion, fibre reinforcement, and mechanical interlocking, at lower densities. Concurrently, anodizing treatment consistently enhances interfacial adhesion, thus promoting stronger bonding and progressive predominantly cohesive failure. The optimized

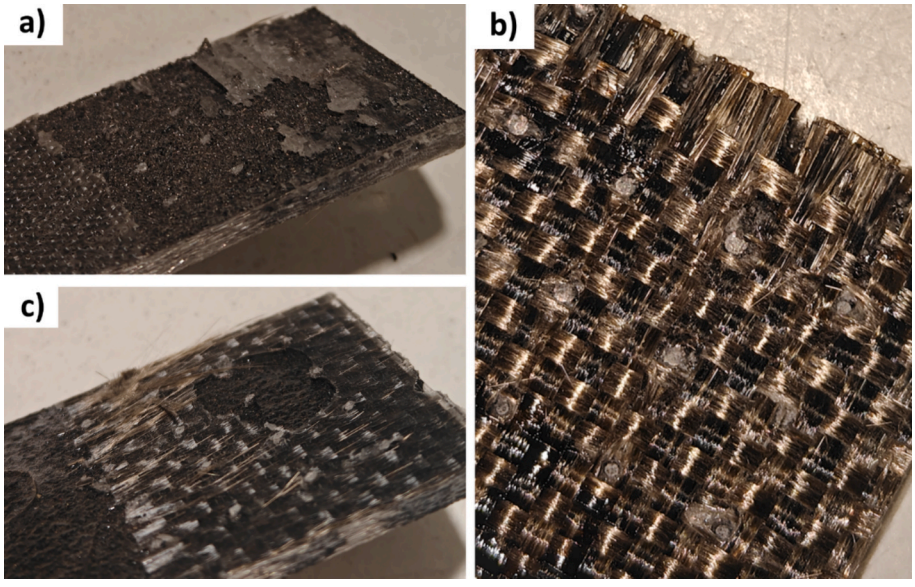

Fig. 14. Rupture surfaces of a) 4-AB; b) 4-AN composite substrate; c) 4-AN. Dimensional details are consistent with those provided in Figs. 1–2.

4-AN configuration emerged as the most effective combination, providing robust evidence for the importance of a tailored pin distribution and surface treatment in improving the structural integrity of multi-material joints.

4. Conclusions

This study investigated the effect of macroscopic pin distribution and anodizing on the mechanical strength of co-bonded joints between additively manufactured AlSi10Mg aluminium alloy substrates and basalt fibre-reinforced epoxy composites. The results from the experimental analysis, specifically tailored to the mechanical interlocking case, indicated that pin density should be carefully optimized in relation to the fabric areal weight used as reinforcement of the composite. In particular, an excessively high pin density should be avoided, as it prevents the composite from fully penetrating the interlocking features, thereby limiting joint strength. Conversely, tailored pin density promotes effective composite infiltration and mechanical interlocking within the matrix, resulting in higher joint strength. Among the tested configurations, the 4 × 4 exhibited the best performance with respect to the basalt fabric used, enhancing fibre interlocking and shifting the failure mode from predominantly adhesive to predominantly cohesive. Nonetheless, this effect showed a certain variability, depending on manufacturing process conditions.

Anodizing using sulfuric acid resulted to be a promising post-processing treatment that can enhance the corrosion resistance of additively manufactured aluminium thanks to the formation of a porous oxide layer, which protects the metallic substrate from an aggressive environment. The results also demonstrated that this treatment consistently improved adhesion and interlocking performances, leading to more robust and process-independent joint behaviour. All anodized samples (PIN-AN) exhibited higher strength, larger displacement at failure, and a predominantly cohesive fracture mode compared to the as-built ones (PIN-AB).

In conclusion, the integration of optimized macroscopic interlocking structures with electrochemical surface treatments enabled superior composite infiltration and fibre interlocking, together with enhanced interfacial adhesion and controlled fracture progression. This combined synergy is therefore essential to improve the mechanical and durability properties of hybrid metal-composite joints. These results are particularly useful for the development of lightweight, high-performance structures applied in aerospace, automotive, and other critical applications.

CRediT authorship contribution statement

Riccardo Miranda: Writing – original draft, Methodology, Investigation. **Federica Valenza:** Writing – original draft, Methodology, Investigation, Visualization. **Francesco Di Franco:** Validation, Resources. **Monica Santamaria:** Validation, Resources. **Alberta Aversa:** Writing – review & editing, Supervision. **Eleonora Atzeni:** Writing – review & editing, Supervision, Funding acquisition. **Sara Biamino:** Writing – review & editing, Supervision, Funding acquisition. **Fabrizio Sarasini:** Funding acquisition. **Vincenzo Fiore:** Writing – review & editing, Supervision, Funding acquisition.

Declaration of competing interest

The authors declare the following financial interests/personal relationships which may be considered as potential competing interests: [Fabrizio Sarasini reports financial support was provided by MUR (Ministero dell'Università e della Ricerca). If there are other authors, they declare that they have no known competing financial interests or personal relationships that could have appeared to influence the work reported in this paper.].

Acknowledgments

The research was funded by MUR (Ministero dell'Università e della Ricerca) under the grant scheme PRIN2020 with the project TARGET "addiTive mAnufactuRing for liGhtwEight joinTs" (grant number 2020E3XL47). The authors are grateful to Professor Alessandro Salmi for his valuable support in the visualization and preparation of the images included in this study.

Data availability

Data will be made available on request.

References

[1] J. Su, X. Wang, C. Tan, S.L. Sing, S. Liang, X. Zhang, Y. Zhao, B. Chen, X. Song, Directionally induced high-density secondary interaction for enhancing the bonding reliability of titanium alloy and CFRTP via functional Schiff base-contained polymer, Compos. B Eng. 275 (2024) 111316, https://doi.org/10.1016/j.compositesb.2024.111316.
[2] S.F. Tseng, Y.S. Chen, T.W. Gao, C.C. Kuo, Investigation of laser-patterned biomimetic microstructures on CFRP and AA5052 surfaces to enhance their single-lap bonding strength, Compos. Part A Appl. Sci. Manuf. 178 (2024) 107980, https://doi.org/10.1016/j.compositesa.2023.107980.
[3] F. Lambiase, S.I. Scipioni, C.J. Lee, D.C. Ko, F. Liu, A state-of-the-art review on advanced joining processes for metal-composite and metal-polymer hybrid structures, Materials 14 (2021) 1890, https://doi.org/10.3390/ma14081890.
[4] A. Galińska, C. Galiński, Mechanical joining of fibre reinforced polymer composites to metals—A review. Part II: riveting, clinching, non-adhesive form-locked joints, pin and loop joining, Polymers (Basel) 12 (2020) 1681, https://doi.org/10.3390/polym12081681.
[5] S.B. Inverarity, R. Das, A.P. Mouritz, Composite-to-metal joining using interference fit micropins, Compos. Part A Appl. Sci. Manuf. 156 (2022) 106895, https://doi.org/10.1016/j.compositesa.2022.106895.
[6] T. Bagnato, A.R. Ravindran, A. Mirabedini, R.B. Ladani, E. Kandare, A.C. Orifici, P. Chang, J. Wang, A.P. Mouritz, Superior interfacial toughening of hybrid metal-composite structural joints using 3D printed pins, Compos. Part A Appl. Sci. Manuf. 168 (2023) 107479, https://doi.org/10.1016/j.compositesa.2023.107479.
[7] N.T. Tuli, S. Khatun, A. Bin Rashid, Unlocking the future of precision manufacturing: a comprehensive exploration of 3D printing with fiber-reinforced composites in aerospace, automotive, medical, and consumer industries, Heliyon 10 (2024) e27328, https://doi.org/10.1016/j.heliyon.2024.e27328.
[8] Y. Song, Y. Ghafari, A. Asefnejad, D. Toghraie, An overview of selective laser sintering 3D printing technology for biomedical and sports device applications: processes, materials, and applications, Opt. Laser Technol. 171 (2024) 110459, https://doi.org/10.1016/j.optlastec.2023.110459.
[9] C. Buchanan, L. Gardner, Metal 3D printing in construction: a review of methods, research, applications, opportunities and challenges, Eng. Struct. 180 (2019) 332–348, https://doi.org/10.1016/j.engstruct.2018.11.045.
[10] A.A. Elhadad, A. Rosa-Sainz, R. Cañete, E. Peralta, B. Begines, M. Balbuena, A. Alcudia, Y. Torres, Applications and multidisciplinary perspective on 3D printing techniques: recent developments and future trends, Mater. Sci. Eng.: R: Rep. 156 (2023) 100760, https://doi.org/10.1016/j.mser.2023.100760.
[11] D. Woitun, M. Roderus, T. Bein, E. Kroner, Precise laser structures as a tool to understand metal-polymer joints, J. Laser Appl. 32 (2020), https://doi.org/10.2351/7.0000060.
[12] D. Xu, K. Fu, C. Sang, R. Chen, P. Chen, Y. Lu, D. Zhu, Q. Xu, J. Cheng, Improving interfacial microstructure and mechanical properties of ODS-W/Cu joints via anodization treatment and spark plasma sintering, J. Nucl. Mater. 601 (2024) 155351, https://doi.org/10.1016/j.jnucmat.2024.155351.
[13] G. Scampone, G. Timelli, Anodizing Al–Si foundry alloys: a critical review, Adv. Eng. Mater. 24 (2022), https://doi.org/10.1002/adem.202101480.
[14] K. Schimanski, A. von Hehl, H.-W. Zoch, Failure behavior of diffusion bonded transition structures for integral FRP-aluminum compounds, Procedia Mater. Sci. 2 (2013) 189–196, https://doi.org/10.1016/j.mspro.2013.02.023.
[15] N. Sarantinos, V. Kostopoulos, G. Di Vita, G. Campoli, L. Bricout, Micro-pins: the next step in composite–composite and metal–composite joining, CEAS Space J. 11 (2019) 351–358, https://doi.org/10.1007/s12567-019-00251-1.
[16] P.N. Parkes, R. Butler, J. Meyer, A. de Oliveira, Static strength of metal-composite joints with penetrative reinforcement, Compos. Struct. 118 (2014) 250–256, https://doi.org/10.1016/j.compstruct.2014.07.019.
[17] D.P. Graham, A. Rezai, D. Baker, P.A. Smith, J.F. Watts, The development and scalability of a high strength, damage tolerant, hybrid joining scheme for composite–metal structures, Compos. Part A Appl. Sci. Manuf. 64 (2014) 11–24, https://doi.org/10.1016/j.compositesa.2014.04.018.
[18] A. Marques, Â. Cunha, M. Gasik, O. Carvalho, F.S. Silva, F. Bartolomeu, Inconel 718–copper parts fabricated by 3D multi-material laser powder bed fusion: a novel technological and designing approach for rocket engine, Int. J. Adv. Manuf. Technol. 122 (2022) 2113–2123, https://doi.org/10.1007/s00170-022-10011-x.
[19] W. Zhao, J. Qiu, E. Sakai, H. Wu, H. Feng, S. Guo, H. Wu, High bonding strength of polyphenylene sulfide-aluminum alloy composite structure achieved by constant

current anodizing in tartaric acid, Int. J. Adhes. Adhes. 130 (2024), https://doi.org/10.1016/j.ijadhadh.2024.103632.
[20] N.M. André, A. Bouali, E. Maawad, P. Staron, J.F. dos Santos, M.L. Zheludkevich, S. T. Amancio-Filho, Corrosion behavior of metal-composite hybrid joints: Influence of precipitation state and bonding zones, Corros. Sci. 158 (2019) 108075, https://doi.org/10.1016/j.corsci.2019.07.002.
[21] R.I. Revilla, H. Terryn, I. De Graeve, Role of Si in the anodizing behavior of Al-Si alloys: additive manufactured and cast Al-Si10-Mg, J. Electrochem. Soc. 165 (2018) C532–C541, https://doi.org/10.1149/2.1301809jes.
[22] R.I. Revilla, D. Verkens, G. Couturiaux, L. Malet, L. Thijs, S. Godet, I. De Graeve, Galvanostatic anodizing of additive manufactured Al-Si10-Mg alloy, J. Electrochem. Soc. 164 (2017) C1027–C1034, https://doi.org/10.1149/2.1121714jes.
[23] V. Fiore, T. Scalici, G. Di Bella, A. Valenza, A review on basalt fibre and its composites, Compos. B Eng. 74 (2015) 74–94, https://doi.org/10.1016/j.compositesb.2014.12.034.
[24] B. Wei, H. Cao, S. Song, Tensile behavior contrast of basalt and glass fibers after chemical treatment, Mater. Des. 31 (2010) 4244–4250, https://doi.org/10.1016/j.matdes.2010.04.009.
[25] F. Sarasini, J. Tirillò, M.C. Seghini, Influence of thermal conditioning on tensile behaviour of single basalt fibres, Compos. B Eng. 132 (2018) 77–86, https://doi.org/10.1016/j.compositesb.2017.08.014.
[26] N. Gadlegaonkar, P.J. Bansod, A. Lakshmikanthan, K. Bhole, A Review on additively manufactured AlSi10Mg alloy: mechanical, tribological, and microstructure properties, J. Mines Metals Fuels (2025) 87–101, https://doi.org/10.18311/jmmf/2025/46621.
[27] J. Moritz, P. Götze, T. Schiefer, L. Stepien, A. Klotzbach, J. Standfuß, E. López, F. Brückner, C. Leyens, Additive manufacturing of titanium with different surface structures for adhesive bonding and thermal direct joining with fiber-reinforced polyether-ether-ketone (PEEK) for lightweight design applications, Metals (Basel) 11 (2021) 265, https://doi.org/10.3390/met11020265.
[28] L. Saitta, V. Prasad, C. Tosto, N. Murphy, A. Ivankovic, G. Cicala, G. Scarselli, Characterization of biobased epoxy resins to manufacture eco-composites showing recycling properties, Polym. Compos. 43 (2022) 9179–9192, https://doi.org/10.1002/pc.27095.
[29] S. Dattilo, G. Cicala, P.M. Riccobene, C. Puglisi, L. Saitta, Full Recycling and re-use of bio-based epoxy thermosets: chemical and thermomechanical characterization of the recycled matrices, Polymers (Basel) 14 (2022) 4828, https://doi.org/10.3390/polym14224828.
[30] L. Saitta, G. Rizzo, C. Tosto, G. Cicala, I. Blanco, E. Pergolizzi, R. Ciobanu, G. Recca, Chemical recycling of fully recyclable bio-epoxy matrices and reuse strategies: a cradle-to-cradle approach, Polymers (Basel) 15 (2023), https://doi.org/10.3390/polym15132809.
[31] M.-G. Song, J.-H. Kweon, J.-H. Choi, J.-H. Byun, M.-H. Song, S.-J. Shin, T.-J. Lee, Effect of manufacturing methods on the shear strength of composite single-lap bonded joints, Compos. Struct. 92 (2010) 2194–2202, https://doi.org/10.1016/j.compstruct.2009.08.041.
[32] F. Valenza, A. Aversa, S. Biamino, E. Atzeni, A. Salmi, R. Miranda, F. Mazzara, V. Fiore, Influence of production systems and anodizing treatments on additively manufactured mechanical interlocking structures, in: Book of Abstracts of the XIV INSTM Conference, Cagliari, 2024, p. 201. https://hdl.handle.net/11583/2992349.
[33] B. Hirschorn, M.E. Orazem, B. Tribollet, V. Vivier, I. Frateur, M. Musiani, Determination of effective capacitance and film thickness from constant-phase-element parameters, Electrochim. Acta 55 (2010) 6218–6227, https://doi.org/10.1016/j.electacta.2009.10.065.
[34] A. Zaffora, F. Di Franco, M. Santamaria, H. Habazaki, F. Di Quarto, The influence of composition on band gap and dielectric constant of anodic Al-Ta mixed oxides, Electrochim. Acta 180 (2015) 666–678, https://doi.org/10.1016/j.electacta.2015.08.068.
[35] T. Dhilipkumar, M. Rajesh, Influence of manufacturing process and GFRP pin loading on shear and dynamic behaviour of composite joints, J. Adhes. 99 (2023) 538–557, https://doi.org/10.1080/00218464.2022.2025782.
[36] W.S. de Carvalho, J. Draper, T. Terrazas-Monje, A. Toumpis, A. Galloway, S. T. Amancio-Filho, Fatigue life assessment and fracture mechanisms of additively manufactured metal-fiber reinforced thermoplastic hybrid structures produced via ultrasonic joining, J. Mater. Res. Technol. 26 (2023) 5716–5730, https://doi.org/10.1016/j.jmrt.2023.08.305.